GFZ
Helmholtz-Zentrum
POTSDAM

Originally published as:

Klemann, V., Wolf, D. (2005): The eustatic reduction of shoreline diagrams: implications for the inference of relaxation-rate spectra and the viscosity stratification below Fennoscandia. - Geophysical Journal International, 162, 1, pp. 249—256.

DOI: http://doi.org/10.1111/j.1365-246X.2005.02637.x

Geophys. J. Int. (2005) **162,** 249–256 doi: 10.1111/j.1365-246X.2005.02637.x

The eustatic reduction of shoreline diagrams: implications for the inference of relaxation-rate spectra and the viscosity stratification below Fennoscandia

Volker Klemann[1] and Detlef Wolf[1,2]

[1] *GeoForschungsZentrum Potsdam, Kinematics and Dynamics of the Earth, Telegrafenberg,* D-14473 *Potsdam, Germany. E-mail: volkerk@gfz-potsdam.de*
[2] *University of Stuttgart, Geodetic Institute, Geschwister-Scholl-Str. 24D,* D-70174 *Stuttgart, Germany*

Accepted 2005 March 14. Received 2005 February 18; in original form 2003 July 14

SUMMARY

One of the main objectives of quantifying glacial-isostatic adjustment is to infer the viscosity of the Earth. An efficient method of determining this parameter is based on the inversion of the observational relaxation-rate spectrum (RRS) constructed from a shoreline diagram representing the relative sea level heights at discrete past time epochs along a given profile. The advantage of using the observational RRS for the inversion is that it is largely insensitive to the Pleistocene ice sheet geometry and history. Implicit assumptions of the method are: the approximate radius and centre of the ice sheet are known, the shorelines are directed to the former ice sheet centre and refer predominantly to the period after deglaciation.

So far, a drawback of the method has been that only a small number of shoreline diagrams have been published and only one diagram has been used to determine an RRS. To overcome this, we propose a simple method of constructing shoreline diagrams from sea level indicators (SLIs) and apply it to a set of SLIs for the Oslo Fjord area. Considering a total of three shoreline diagrams for Fennoscandia, we then demonstrate the robustness of the observational RRS inferred with respect to the diagram considered. We also show that the previous neglect of the eustatic reduction when inferring the observational RRS from a given shoreline diagram is only slightly reflected in the viscosity stratification determined.

Key words: eustatic reduction, Fennoscandia, glacial-isostatic adjustment, mantle viscosity, sea level change.

1 INTRODUCTION

The conventional method of inverting for the viscosity stratification of the Earth from glacial-isostatic adjustment observations is to use an iterative strategy, where the ice sheet model and the earth model are varied alternately in order to fit relative sea level data (e.g. Tushingham & Peltier 1991; Breuer & Wolf 1995; Kaufmann & Wolf 1996; Lambeck *et al.* 1998; Kaufmann & Lambeck 2002). The disadvantage of this procedure is the large number of free parameters and, thus, the difficulties in controlling the inversion procedure. In particular, for each step, the ice sheet model inferred depends on the earth model inferred at the previous step and *vice versa*.

An alternative method of inferring the viscosity stratification of the Earth is the use of the relaxation-rate spectrum (RRS) of glacial-isostatic adjustment derived from a given shoreline diagram, as originally implemented by McConnell (1968). A shoreline diagram represents relative sea level heights at different postglacial time epochs as functions of distance from an assumed ice-load centre, whereas the observational RRS gives the exponential decay rates associated with the Legendre spectra of the individual sea level heights. Because the amplitudes of the exponential functions are removed in this procedure, the dependence of the observational RRS on the Pleistocene ice sheet is also largely removed (Mitrovica & Peltier 1993).

The conventional shoreline diagram used for the inference of the viscosity stratification below Fennoscandia refers to a profile directed to the SE from the former Fennoscandian ice sheet centre (Fig. 1). It originates in the compilation of Sauramo (1958) and was later interpreted in terms of mantle viscosity by McConnell (1968), Parsons (1972), Cathles (1975) and Mitrovica & Peltier (1993) (see Wolf 1996). Sauramo's diagram was subsequently revised in a series of publications by Donner reviewed in Donner (1995). The new shoreline diagram was rigorously discussed by Wieczerkowski *et al.* (1999). So far, shoreline diagrams different from the SE profile have not been used for the inference of the viscosity stratification. This goes back to McConnell (1968), who ruled out other shorelines in view of their poor quality. In the present study, we consider two additional Fennoscandian profiles. The first is directed to the NW. The associated shoreline diagram was constructed by Kjemperud (1986), who used sea level indicators (SLIs) from isolation basins

© 2005 RAS

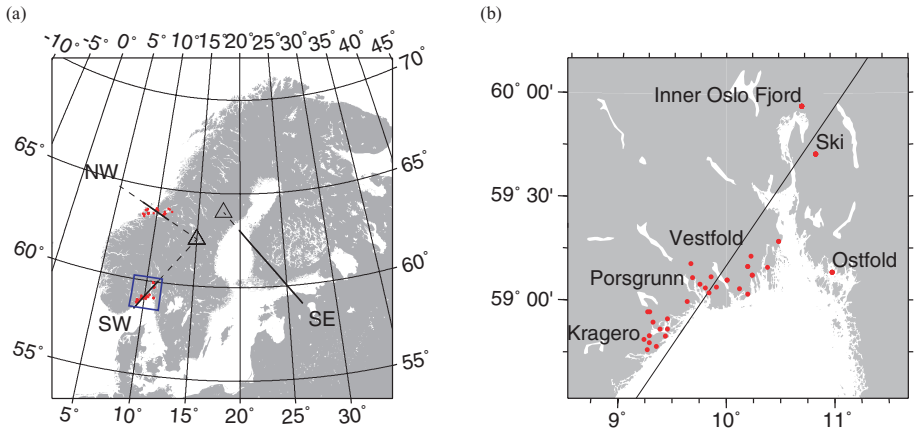

Figure 1. (a) Locations of shoreline profiles considered. The SW profile is located in the Oslo Fjord area, the NW profile in the Trondheims Fjord area and the SE profile in central Fennoscandia. The triangles denote the assumed ice-load centres. Bold lines show sections where data exist on the profiles. (b) Locations of SLIs used for the construction of the shoreline diagram for the SW profile.

in the Trondheims Fjord area. (The term SLI refers to a sample indicative of postglacial sea level, for which location, height and age have been determined (e.g. Shennan *et al.* 2000).) The second profile is directed to the SW and the associated shoreline diagram will be newly constructed on the basis of SLIs from isolation basins in the Oslo Fjord area (Fig. 1).

When inferring the observational RRS in previous studies, no eustatic reduction was usually applied to the relative sea level heights. This reduction accounts for a sea level rise as a result of mass redistribution between the Pleistocene ice sheets and the oceans during deglaciation. The argument used by Wieczerkowski (1999) for this neglect was that a uniform sea level rise has no influence on the inference of the RRS, because it corresponds to a zero-degree contribution. This argument is based on the assumption that the orthogonality of Legendre functions holds for the inference of the RRS. In contrast to this, McConnell (1968) had applied some reduction by subtracting the height of the untilted portion of the shoreline near the periphery of the deformed area. In the following, we will allow for the eustatic contribution in form of a linear sea level rise according to Fleming *et al.* (1998), where the assumption of linearity is motivated by the attempt to retain only the first-order features of the eustatic reduction.

2 CONSTRUCTION OF SHORELINE DIAGRAM

In the present study, a shoreline diagram represents a set of eustatically reduced relative sea level heights for selected time epochs given as functions of distance on a profile from an assumed ice sheet centre. For the eustatic reduction, we use the eustatic sea level curve published by Fleming *et al.* (1998). The three shoreline profiles considered are shown in Fig. 1(a). As a reference, we use the SE profile, for which the shoreline diagram constructed by Donner (1995) is based on palaeoshorelines and SLIs. As a consequence of the profile length of ∼500 km, its quality for inferring the RRS is good. The NW profile was compiled by Kjemperud (1986) and is based on 45 SLIs. It is located in the Trondheims Fjord area and its length is only ∼100 km. The SW profile is based on a newly compiled set of 61 SLIs. It is located in the Oslo Fjord area and has a length of ∼110 km. The SLIs used for this profile refer to dated isolation events for the inner Oslo Fjord (Hafsten 1979), Kragero (Stabell 1980), Ostfold (Hafsten 1979), Porsgrunn (Stabell 1980), Ski (Sørensen 1979) and Vestfold (Henningsmoen 1979) (Fig. 1b; Table 1).

For the construction of the new shoreline diagram associated with the SW profile, we follow the method suggested by Kjemperud (1986). First, a profile extending from his assumed ice sheet centre at 62.5°N, 15°E, with an orientation that minimizes the angular distances of the I SLIs considered from the profile, is determined (Fig. 1). Denoting the relative sea level height of the ith SLI by $h_{\mathrm{RSL}}(x_i, t_i)$, where x_i and t_i are its distance from the ice sheet centre and its ^{14}C age, respectively, the shoreline diagram is then constructed as follows. We select ages, t_k, where $t_k = 4.0, 6.0, 8.0, 9.0$ ka, and, for each t_k, determine the best-fitting twisted plane

$$h_{\mathrm{RSL}}(x, t) = b_0(t_k) + b_1(t_k)\,x + b_2(t_k)\,t + b_3(t_k)\,x\,t \qquad (1)$$

to $h_{\mathrm{RSL}}(x_i, t_i)$ by a least-squares fit (Fig. 2), where x is the distance on the profile from the ice sheet centre, $t_i \in [t_k - \Delta t, t_k + \Delta t]$ for $i = 1, \ldots, I$, $\Delta t = 1$ ka, and $b_0(t_k), \ldots, b_2(t_k)$ are constants. The kth shoreline of the diagram is the intersection of the kth best-fitting plane with the plane $t = t_k$:

$$h_{\mathrm{RSL}}(x, t_k) = [b_0(t_k) + b_2(t_k)\,t_k] + [b_1(t_k) + b_3(t_k)\,t_k]\,x. \qquad (2)$$

Following this, the ^{14}C ages, t_k, are converted to time epochs before present (BP) in calendar years using the program CALIB 4.1 (Stuiver & Reimer 1993). For the converted time epochs BP, we find $t_k = 4.7, 7.0, 9.3, 10.5$ ka. Finally, the eustatically reduced relative sea level height is calculated:

$$h_{\mathrm{red}}(x, t_k) = h_{\mathrm{RSL}}(x, t_k) - h_{\mathrm{EU}}(t_k), \qquad (3)$$

with $h_{\mathrm{EU}}(t_k)$ the eustatic sea level rise since t_k according to Fleming *et al.* (1998). Fig. 3 shows $h_{\mathrm{EU}}(t_k)$ and Fig. 4 the eustatically reduced shoreline diagram for the SW profile. In this figure, three supporting points with the associated standard deviations are chosen for each shoreline. In order to stabilize the inference of the observational RRS, we add sea level heights at the ice-load centres with a standard deviation of 10 per cent (Wieczerkowski *et al.* 1999). The central height values are not crucial as long as they are positive and monotonically decreasing to zero for the present time epoch.

Table 1. SLIs used for the construction of the SW shoreline diagram. The geographical coordinates are in the decimal system, h_{RSL} is in m above present-day sea level, and the ^{14}C age in a is referred to the calendar year 1950 and based on a half-life of 5570 a. Ages without laboratory reference number, Lab., are based on pollen analysis. All values refer to isolation events, with an uncertainty in h_{RSL} of $\simeq$1 m, and are taken from Stabell (1980) [1], Hafsten (1979) [2], Sørensen (1979) [3], Henningsmoen (1979) [4].

No.	Curve	Long.	Lat.	h_{RSL}	Lab.	C14 age
1	Kragero[1]	9.283	58.8	82.0	T–2415	9180 ± 340
2	Kragero	9.267	58.95	99.0	T–1968	9040 ± 210
3	Kragero	9.233	58.817	50.5	T–1967	8820 ± 300
4	Kragero	9.433	58.833	43.0	T–1966	8500 ± 180
5	Kragero	9.283	58.95	38.0	T–1965	7720 ± 200
6	Kragero	9.317	58.9	28.6	T–1964	6270 ± 130
7	Kragero	9.45	58.917	27.5	T–1853	5860 ± 290
8	Kragero	9.267	58.767	18.5	T–1852	4340 ± 180
9	Kragero	9.35	58.783	15.0	T–2414	3830 ± 280
10	Kragero	9.45	58.867	14.9	T–1851	3070 ± 170
11	Kragero	9.383	58.867	10.5	T–1963	2750 ± 240
12	Kragero	9.283	58.833	8.4	T–1850	2630 ± 180
13	Ostfold[2]	10.99	59.14	185.0		10240 ± 250
14	Ostfold	10.99	59.14	115.0		9350 ± 250
15	Ostfold	10.99	59.14	60.0		8140 ± 250
16	Ostfold	10.99	59.14	20.0		5000 ± 250
17	Ostfold	10.99	59.14	8.0		2480 ± 250
18	Porsgrunn[1]	9.633	59.0	58.1		8850 ± 250
19	Porsgrunn	9.75	59.083	47.0	T–1732	8000 ± 270
20	Porsgrunn	9.8	59.067	31.9	T–1849	5900 ± 240
21	Porsgrunn	9.667	59.183	19.5	T–1740	3750 ± 150
22	Porsgrunn	9.683	59.117	7.4	T–2120	2360 ± 110
23	Ski[3]	10.85	59.71	186.0	T–1623	10400 ± 250
24	Ski	10.85	59.71	146.0	T–1319	9600 ± 150
25	Ski	10.85	59.71	120.0	T–1528	9200 ± 350
26	Ski	10.85	59.71	80.0	T–1837	8800 ± 270
27	Ski	10.85	59.71	80.0	T–604	8100 ± 110
28	Ski	10.85	59.71	53.0	T–1624	6400 ± 450
29	Ski	10.85	59.71	44.0	T–1838	5500 ± 100
30	Ski	10.85	59.71	24.0	T–1529	3400 ± 140
31	Vestfold[4]	9.855	59.12	142.7	T–377	10280 ± 90
32	Vestfold	10.23	59.22	87.7	T–2436	9340 ± 140
33	Vestfold	9.905	59.07	62.5	T–88	8710 ± 280
34	Vestfold	10.005	59.105	50.1	T–241 B	8000 ± 300
35	Vestfold	10.005	59.105	50.1	T–241 A	7900 ± 250
36	Vestfold	10.2	59.17	31.5	T–2433	5570 ± 200
37	Vestfold	10.2	59.17	31.5	T–2432	5460 ± 230
38	Vestfold	10.12	59.063	26.1	T–2140	5280 ± 110
39	Vestfold	10.49	59.29	26.1	T–2435	4340 ± 130
40	Vestfold	10.49	59.29	26.1	T–2434	4120 ± 150
41	Vestfold	10.385	59.165	13.0	T–2141	2920 ± 100
42	Vestfold	10.24	59.128	7.7	T–29	2425 ± 85
43	Vestfold	10.198	59.038	11.4	T–89 B	2400 ± 150
44	Vestfold	10.24	59.128	7.7	T–30	2260 ± 145
45	Vestfold	9.835	59.042	3.4	T–2144	1200 ± 110
46	Inner Oslo F.[2]	10.72	59.94	208.0		9700 ± 250
47	Inner Oslo F.	10.72	59.94	196.0		9600 ± 250
48	Inner Oslo F.	10.72	59.94	191.0		9500 ± 250
49	Inner Oslo F.	10.72	59.94	182.0		9500 ± 250
50	Inner Oslo F.	10.72	59.94	162.0		9400 ± 250
51	Inner Oslo F.	10.72	59.94	143.0		9300 ± 250
52	Inner Oslo F.	10.72	59.94	111.0		9000 ± 250
53	Inner Oslo F.	10.72	59.94	97.0		8800 ± 250
54	Inner Oslo F.	10.72	59.94	86.0		8500 ± 250
55	Inner Oslo F.	10.72	59.94	71.0		8200 ± 250
56	Inner Oslo F.	10.72	59.94	60.0		7800 ± 250
57	Inner Oslo F.	10.72	59.94	56.0		7700 ± 250
58	Inner Oslo F.	10.72	59.94	42.0		6800 ± 250
59	Inner Oslo F.	10.72	59.94	14.0		3800 ± 250
60	Inner Oslo F.	10.72	59.94	12.0		3500 ± 250
61	Inner Oslo F.	10.72	59.94	8.0		2500 ± 250

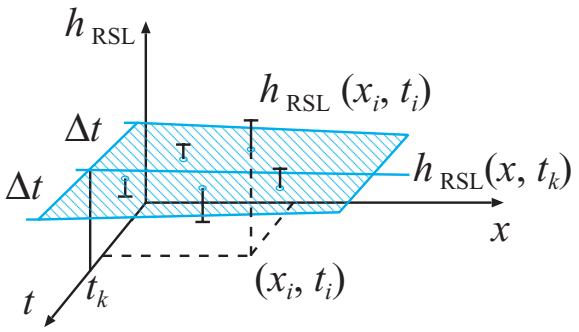

Figure 2. Construction of twisted plane from projected SLIs.

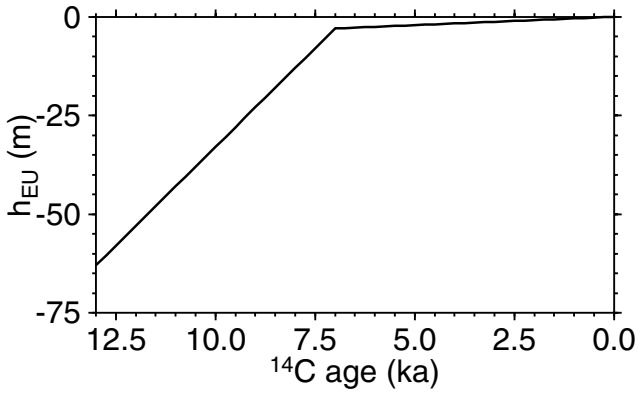

Figure 3. Eustatic reduction after Fleming *et al.* (1998) used for shoreline diagrams.

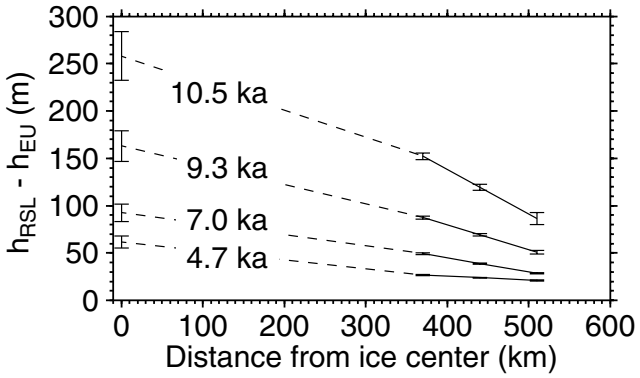

Figure 4. Eustatically reduced shoreline diagram constructed for the SW profile. The dashed lines indicate regions where no data are available.

3 INFERENCE OF OBSERVATIONAL RRS

Except for the eustatic reduction applied to the shoreline diagrams, the procedure of inferring the observational RRS from a shoreline diagram adopted follows the Bayesian approach of Wieczerkowski *et al.* (1999). It consists of two steps. First, for each time epoch, t_k, the eustatically reduced relative sea level height, $h_{\rm red}(x_j)$, is expanded in the Legendre domain up to degree 120:

$$h_{\rm red}(x, t_k) = \sum_l a_l(t_k)\, P_l(x), \tag{4}$$

with a_l the Legendre coefficient of the lth Legendre function, P_l. Because of the finite length of the profile (Fig. 4), the inversion for the Legendre coefficients is underdetermined. As suggested by Wieczerkowski *et al.* (1999), we therefore use a damped least-squares fitting procedure allowing for a correlation length of $\lambda = 6$ between neighbouring Legendre degrees, m, n, where the elements of the *a priori* covariance matrix are

$$V_{mn}^{\rm apr} = \sigma_m \sigma_n e^{|m-n|/\lambda}, \tag{5}$$

with $\sigma_l = 0.42 \exp(-0.033\, l)$ as an *a priori* weight for the coefficients a_l appropriate to the Fennoscandian ice load. Following this, for each Legendre degree, l, an exponential function of the form

$$a_l(t_k) = A_l \left[e^{-(t_k - t_{\rm PT})\alpha_l} - 1 \right], \quad k = 1, \ldots, 4, \tag{6}$$

is fitted, where A_l is the amplitude, α_l the relaxation rate and $t_{\rm PT}$ the present time epoch. Using, for both steps, a least-squares fit, the uncertainties in the determination of the sea level heights are propagated into the observational RRS. It is important to note that, in the following, only the relaxation rates and not the amplitudes will be used. This is because the amplitudes are also influenced by the ice sheet model adopted.

The resulting observational RRS inferred for the three profiles are in close agreement. Fig. 5 shows the relaxation rates as functions of the Legendre degree for $l = 10$–80. The RRS for the SW profile is smooth, with an average value of ∼0.25 l/ka. The error bars are increasing with Legendre degree. Beyond approximately $l = 45$, the uncertainties become too large. The RRS for the NW profile shows a similar behaviour. Here, the uncertainties are significant also for low degrees and the spectrum is resolved only in the range $l = 12$–67. The relaxation rates for the SE profile are slightly smaller, but the values lie within the uncertainties for the other two profiles. In contrast to them, the SE profile also shows some resolution for $l = 60$–80 even though the uncertainties are rather large. The lower right panel of Fig. 5 shows the superposition of the spectra. Although, the differences between the RRS are small, the rates for the SE profile are systematically smaller than the rates for the SW profile and the NW profile for $l = 25$–40. In view of the error bars, however, we cannot conclude that this behaviour suggests lateral viscosity variations, which were suggested by Kaufmann & Wu (2002).

4 IMPLICATIONS OF EUSTATIC REDUCTION ON OBSERVATIONAL RRS

To examine the relevance of the eustatic reduction for the inference of the RRS, we show in Fig. 6 also the spectra inferred for the shoreline diagrams without eustatic reduction. In particular, the spectrum for the SE profile represents that considered by Wieczerkowski *et al.* (1999). Also shown are for each profile the spectra for the eustatically reduced shorelines plotted in Fig. 5. The overall behaviour of the unreduced spectra is similar to that of the eustatically reduced spectra. Only for the degree range $l \leq 20$, we observe a shift to shorter rates, which is most pronounced for the SE profile.

To demonstrate that the application of the eustatic reduction does, in fact, improve the RRS, we perform the following test calculations for the SE profile. We employ the time domain approach to relaxation of a self-gravitating, incompressible, Maxwell-viscoelastic earth model with elastic PREM (Preliminary Reference Earth Model) structure (Martinec 2000), a lithosphere thickness of $h_{\rm L} = 70$ km, an upper-mantle viscosity of $\eta_{\rm UM} = 5 \times 10^{20}$ Pa s and a lower-mantle viscosity of $\eta_{\rm LM} = 2 \times 10^{21}$ Pa s, with the interface at 670 km depth. The earth model is

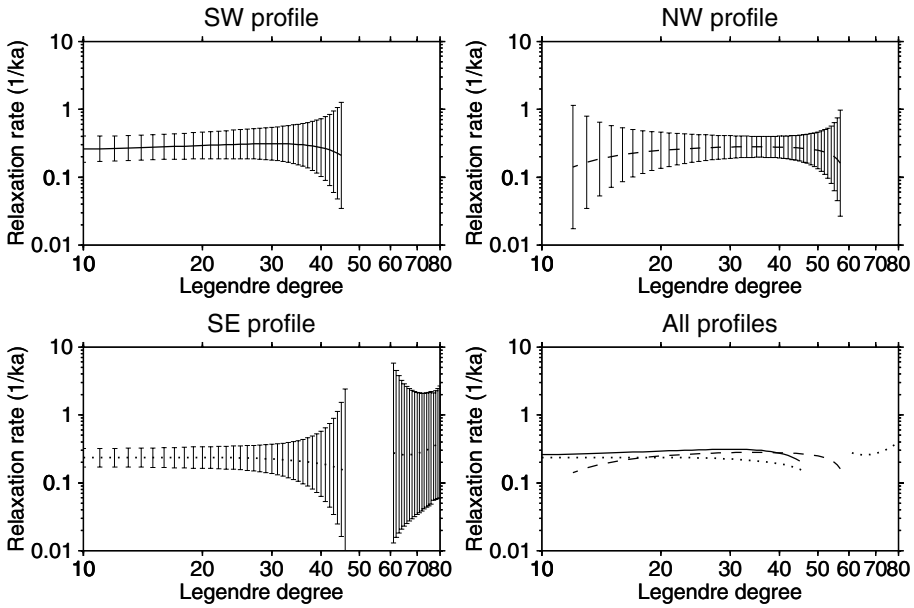

Figure 5. Observational RRS and uncertainties for the eustatically reduced shoreline diagrams associated with the SW profile (solid), the NW profile (dashed) and the SE profile (dotted). The lower right panel shows a superposition of the individual RRS.

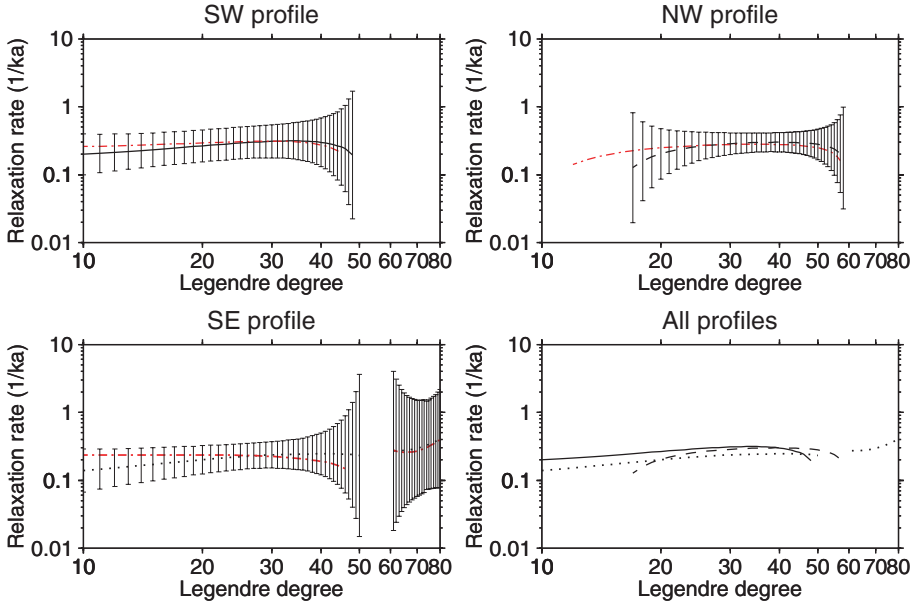

Figure 6. Observational RRS and uncertainties for the eustatically unreduced shoreline diagrams associated with the SW profile (black solid), the NW profile (black dashed) and the SE profile (black dotted). The lower right panel shows a superposition of the individual RRS. Dash-dotted, the corresponding RRS for the eustatically reduced shoreline diagrams are plotted.

combined with a new time domain algorithm for the solution of the sea level equation allowing for the ice–ocean mass balance, geoid-height changes and moving coast lines (Wolf *et al.* 2002; Hagedoorn 2005) following the theory of Milne (1998) and the ice sheet model ICE-3G (Tushingham & Peltier 1991). For the SE profile, we then calculate the following quantities: the relative radial displacement, $u(t) - u(t_{\mathrm{PT}})$, and the relative sea level height, $h^{\mathrm{syn}}_{\mathrm{RSL}}(t) - h^{\mathrm{syn}}_{\mathrm{RSL}}(t_{\mathrm{PT}})$, as direct output of the program. As the third quantity, we calculate $h^{\mathrm{syn}}_{\mathrm{red}} := h^{\mathrm{syn}}_{\mathrm{RSL}} - h_{\mathrm{EU}}$ by applying the eustatic reduction, h_{EU}. In Fig. 7, these quantities are shown for the time epochs chosen by Wieczerkowski *et al.* (1999). The curves for u and $h^{\mathrm{syn}}_{\mathrm{red}}$ roughly coincide for the time epochs 4.85 and 10 ka BP, whereas, for the intermediate time epochs, $h^{\mathrm{syn}}_{\mathrm{red}}$ is between u and $h^{\mathrm{syn}}_{\mathrm{RSL}}$. This difference probably reflects regional geoid-height changes not accounted for by the assumption of a non-gravitating ocean when applying the eustatic reduction.

When calculating the 'observational' RRS from the three quantities (Fig. 8), the spectrum obtained for the relative radial displacement is very close to the synthetic RRS of the earth model used. The same applies to the spectrum for the relative sea level height with eustatic reduction. In contrast to this is the spectrum based on the relative sea level height without eustatic reduction, which is

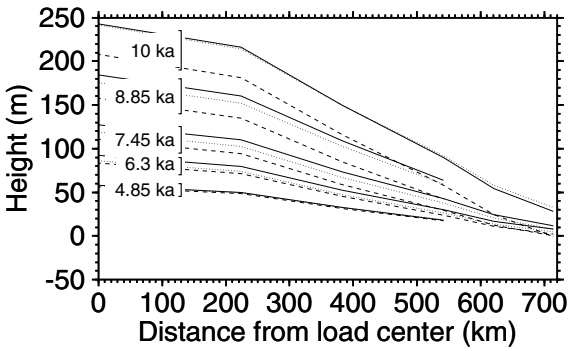

Figure 7. Synthetic shoreline diagrams for the SE profile based on calculations of relative radial displacement (solid), eustatically unreduced relative sea level height (dashed) and eustatically reduced relative sea level height (dotted). Triples of curves for the same time epoch BP are marked by square brackets. The theoretical model used is described in the text.

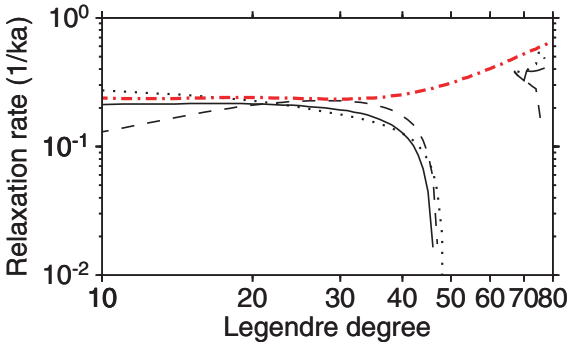

Figure 8. 'Observational' RRS constructed from synthetic shoreline diagrams shown in Fig. 7 for the SE profile based on calculations of relative radial displacement (solid), eustatically unreduced relative sea level height (dashed), eustatically reduced relative sea level height (dotted) and synthetic RRS for the earth model described in the text (dash-dotted).

significantly lower than the synthetic RRS for $l < 20$. This behaviour is also reflected in Fig. 6.

To investigate the implications of the eustatic reduction for the inference of the viscosity stratification, only the SE and SW profiles are considered. (The NW spectrum is ignored, because its difference from the SW spectrum is insignificant and the uncertainties for low degrees are large.)

In the inversion, h_{L}, η_{UM} and η_{LM} are free parameters, with the interface between the upper and lower mantle at 670 km depth. The density and the elastic parameters are kept fixed and correspond to those of the PREM model. Because we use the locally incompressible earth model developed by Martinec *et al.* (2001), its response is governed by a small number of relaxation modes. Thus, the entirely dominant M0 mode is easily identified and the synthetic RRS readily determined. For the inversion, 432 earth models have been considered, with the free parameters varied in the following ranges: $h_{\mathrm{L}} \in [70, 120]$ km, $\eta_{\mathrm{UM}} \in [10^{20}, 10^{21}]$ Pa s and $\eta_{\mathrm{LM}} \in [10^{21}, 4 \times 10^{22}]$ Pa s.

The misfits of the synthetic RRS to the observed RRS for the SE and SW profiles with and without eustatic reduction and for the best-fitting value of h_{L}, respectively, are shown in Fig. 9, where the misfit is parametrized by the variance according to

$$\chi^2 := \sum_l \frac{\left(\alpha_l - \alpha_l^{\mathrm{syn}}\right)^2}{\sigma_l^2}, \tag{7}$$

with α_l^{syn} the relaxation rate for the synthetic RRS and σ_l the associated standard deviation. The grey-shaded areas show the confidence regions according to (Press *et al.* 1992, p. 687) and the error bars show the confidence limits determined from all earth models considered. The minima of the misfit function represent an upper-mantle viscosity of $\sim 5 \times 10^{20}$ Pa s and a lower-mantle viscosity of $\sim 2.4 \times 10^{21}$ Pa s, where the latter is, however, only poorly resolved. This poor resolution is more pronounced for the eustatically unreduced shoreline diagrams, where the contours are almost band shaped. For the SE profile and eustatically reduced shorelines, the range defined by the confidence limits for the lower-mantle viscosity is much smaller. However, because of the limited sensitivity of the response to the viscosity below ~1400 km depth (Mitrovica 1996), this result must be interpreted with care. For the upper-mantle viscosity, the eustatic reduction has almost no influence. The value of ~80 km inferred for the lithosphere thickness is also nearly insensitive to this reduction, where the confidence limits comprise the complete parameter range considered.

5 CONCLUDING REMARKS

The main results of the present study can be summarized as follows.

(i) A simple method of constructing shoreline diagrams from a given set of SLIs has been used to obtain a new shoreline diagram for a profile in the Oslo Fjord region of Fennoscandia.

(ii) The inference of the observational RRS from the classical shoreline diagram in SE Fennoscandia and the inversion of this RRS in terms of a viscosity model has been extended to two additional Fennoscandian shoreline diagrams. The observational RRS for the three profiles are in close agreement and, as a consequence, lead to almost identical viscosity models. This result shows that the RRS is largely insensitive to lateral heterogeneities in the viscosity distribution of the Earth. Such heterogeneities have been suggested for Fennoscandia from seismological (e.g. Babuška *et al.* 1988; Gregersen & Voss 2002) and geothermal (e.g. Pasquale *et al.* 1991) evidence and also from glacial-isostatic adjustment studies (Kaufmann & Wu 2002). The insensitivity found also agrees with the results of Martinec & Wolf (2005), who showed that the resolving power for lateral viscosity variations is rather small on the basis of the RRS for the SE profile.

(iii) The neglect of the eustatic reduction when inferring the observational RRS (Wieczerkowski *et al.* 1999) has been shown to decrease the observational relaxation rate for low Legendre degrees. This agrees with Mitrovica *et al.* (2000), who demonstrated the importance of the eustatic reduction when using postglacial decay times from locations near the former centre of the Laurentide ice sheet for the inference of mantle viscosity. The slightly higher relaxation rates obtained from the eustatically reduced shoreline diagrams correspond to recent results of a joint inversion by Mitrovica & Forte (2004, Fig. 2). A similar shift is observed if the ellipticity of the Fennoscandian ice sheet is considered, which results in an increase of ~0.1 l/ka in the relaxation rates for low degrees for the SE profile (Wieczerkowski *et al.* 1999).

(iv) The resolution of η_{LM} is improved for the eustatically reduced shorelines. However, the optimum value of $\sim 2.4 \times 10^{21}$ Pa s is small if compared with the averaged viscosity of the lower mantle inferred from global studies (Forte & Peltier 1987; Nakada & Lambeck 1989; Mitrovica & Forte 2004). This deviation is a consequence of the limited sensitivity of the response considered in the present study to the lower part of the lower mantle. Whereas the above studies consider the convection process or the far-field

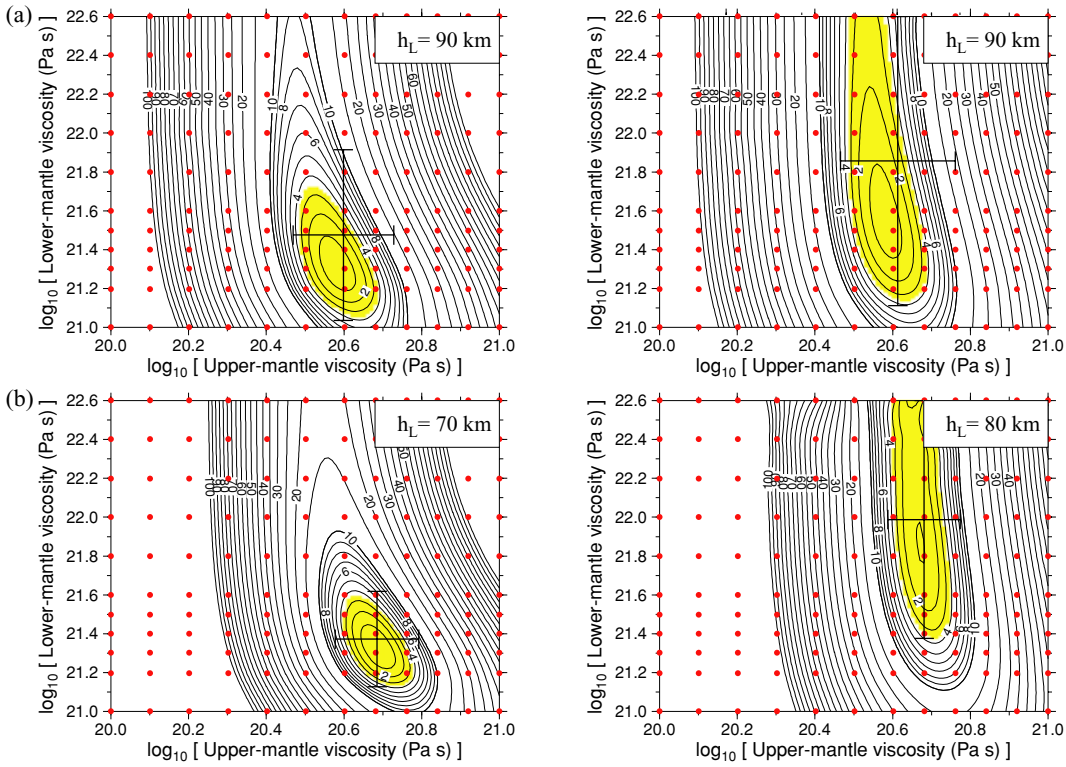

Figure 9. Variance, χ^2, as a function of the free parameters $\eta_{\rm UM}$ and $\eta_{\rm LM}$ for (a) the SW profile and (b) the SE profile. For each profile, the best-fitting value of $h_{\rm L}$ is given. The grey areas show the confidence regions of the misfit, the error bars indicate the confidence limits determined from all earth models considered. The results apply to eustatically reduced relative sea level heights (left) and eustatically unreduced relative sea level heights (right).

glacial-isostatic adjustment and, thus, resolve the whole lower mantle, the sensitivity to viscosity of glacial-isostatic adjustment in Fennoscandia is limited to ∼1400 km in depth (Mitrovica 1996). Considering these limitations, the inferred value is consistent. On the other hand, our value of $\eta_{\rm LM}$ agrees with the average viscosity inferred by Mitrovica & Forte (2004) for the upper part of the lower mantle.

ACKNOWLEDGMENTS

We thank Georg Kaufmann and Jerry Mitrovica for their constructive reviews, which improved the manuscript significantly. This paper is a contribution to the SEAL (Sea-level change) project sponsored by the Hermann von Helmholtz Association of German Research Centres, Federal Ministry of Education and Research (BMBF), Project No. SF2000/13.

REFERENCES

Babuška, V., Plomerová, J. & Pajdušák, P., 1988. Seismologically determined deep lithosphere structure in Fennoscandia, *Geol. Fören. Stockholm Förh.,* **110,** 380–382.

Breuer, D. & Wolf, D., 1995. Deglacial land emergence and lateral upper-mantle heterogeneity in the Svalbard Archipelago—I. First results for simple load models, *Geophys. J. Int.,* **121,** 775–788.

Cathles, L.M., 1975. *The Viscosity of the Earth's Mantle*, Princeton University Press, Princeton.

Donner, R.K., 1995. *The Quaternary History of Fennoscandia*, Cambridge University Press, Cambridge.

Fleming, K., Johnston, P., Zwartz, D., Yokohama, Y., Lambeck, K. & Chappell, J., 1998. Refining the eustatic sea-level curve since the Last Glacial Maximum using far- and intermediate-field sites, *Earth planet. Sci. Lett.,* **163,** 327–342.

Forte, A.M. & Peltier, W.R., 1987. Plate tectonics and aspherical earth structure: the importance of poloidal–toroidal coupling, *J. geophys. Res.,* **92,** 3645–3679.

Gregersen, S. & Voss, P., 2002. Summary of project TOR: delineation of a stepwise, sharp, deep lithosphere transition across Germany–Denmark–Sweden, *Tectonophysics,* **360,** 61–73.

Hafsten, U., 1979. Late and Post-Weichselian shore level changes in South Norway. In: Oele, E., Schüttenhelm, R.T.E. & Wiggers, A.J. (eds), *Acta Univ. Ups., Symp. Univ. Ups. annum quingentesimum celebrantis, Vol. 2: The Quaternary history of the North Sea*, pp. 159–174, University of Uppsala, Uppsala.

Hagedoorn, J. 2005. Glaziale Isostasie and rezente Meeresspiegeländerung, *PhD thesis,* University of Stuttgart, Stuttgart.

Henningsmoen, K.E., 1979. En karbon-datert starandforskyvningskurve fra søndre Vestfold, in *Fortiden i sökelyset*, pp. 239–247, eds Nydal, R., Westin, S., Hafsen, U. & Gulliksen, S., Universitetsforlaget Trondheim, Trondheim.

Kaufmann, G. & Lambeck, K., 2002. Glacial isostatic adjustment and the radial viscosity profile from inverse modeling, *J. geophys. Res.,* **107,** 2280, doi:10.1029/2001JB000941.

Kaufmann, G. & Wolf, D., 1996. Deglacial land emergence and lateral upper-mantle heterogeneity in the Svalbard Archipelago—II. Extended results for high-resolution models, *Geophys. J. Int.,* **127,** 125–140.

Kaufmann, G. & Wu, P., 2002. Glacial isostatic adjustment in Fennoscandia with a three-dimensional viscosity structure as an inverse problem, *Earth planet. Sci. Lett.,* **197,** 1–10.

Kjemperud, A., 1986. Late Weichselian and Holocene shoreline displacement in the Trondjeimsfjord area, central Norway, *Boreas,* **15,** 61–82.

Lambeck, K., Smither, C. & Johnston, P., 1998. Sea-level change, glacial rebound and mantle viscosity for northern Europe, *Geophys. J. Int.,* **134,** 102–144.

McConnell, R.K., 1968. Viscosity of the mantle from relaxation time spectra of isostatic adjustment, *J. geophys. Res.,* **73,** 7089–7105.

Martinec, Z., 2000. Spectral–finite element approach for three-dimensional viscoelastic relaxation in a spherical earth, *Geophys. J. Int.,* **142,** 117–141.

Martinec, Z. & Wolf, D., 2005. Inverting the Fennoscandian relaxation-time spectrum in terms of an axisymmetric viscosity distribution with a lithospheric root, *J. Geodyn.,* **39,** 143–163.

Martinec, Z., Thoma, M. & Wolf, D., 2001. Material versus local incompressibility and its influence on glacial-isostatic adjustment, *Geophys. J. Int.,* **144,** 136–156.

Milne, G.A., 1998. Refining Models of the Glacial Isostatic Adjustment Process, *PhD thesis*, University of Toronto, Toronto.

Mitrovica, J.X., 1996. Haskell [1935] revisited, *J. geophys. Res.,* **94,** 555–569.

Mitrovica, J.X. & Forte, A.M., 2004. A new inference of mantle viscosity based upon joint inversion of convection and glacial isostatic adjustment data, *Earth planet. Sci. Lett.,* **225,** 177–189.

Mitrovica, J.X. & Peltier, W.R., 1993. The inference of mantle viscosity from an inversion of the Fennoscandian relaxation spectrum, *Geophys. J. Int.,* **114,** 45–62.

Mitrovica, J.X., Forte, A.M. & Simons, M., 2000. A reappraisal of postglacial decay times from Richmond Gulf and James Bay, Canada, *Geophys. J. Int.,* **142,** 783–800.

Nakada, M. & Lambeck, K., 1989. Late Pleistocene and Holocene sea-level change in the Australian region and mantle rheology, *Geophys. J.,* **96,** 497–517.

Parsons, B.E., 1972. Changes in the Earth's Shape, *PhD thesis*, University of Cambridge, Cambridge.

Pasquale, V., Verdoya, M. & Chiozzi, P., 1991. Lithospheric thermal structure in the Baltic shield, *Geophys. J. Int.,* **106,** 611–620.

Press, W.H., Teukolsky, S.L., Vetterling, W.T. & Flannery, B.P., 1992. *Numerical Recipes in FORTRAN—The Art of Scientific Computing*, 2nd edn, Cambridge University Press, Cambridge.

Sauramo, M.R., 1958. Die Geschichte der Ostsee, *Ann. Acad. Sci. Fenn., Ser. A3,* **51,** 1–522.

Shennan, I., Lambeck, K., Horton, B., Innes, J., Lloyd, J., McArthur, J., Purcell, T. & Rutherford, M., 2000. Late Devensian and Holocene records of relative sea-level changes in northwest Scotland and their implications for glacio-hydro-isostatic modelling, *Quat. Sci. Rev.,* **19,** 1103–1135.

Sørensen, R., 1979. Late Weichselian deglaciation in the Oslofjord area, south Norway, *Boreas,* **8,** 241–246.

Stabell, B., 1980. Holocene shorelevel displacement in Telemark, southern Norway, *Norsk Geol. Tidskr.,* **60,** 71–81.

Stuiver, M. & Reimer, P.J., 1993. Extended ^{14}C data base and revised CALIB 3.0 ^{14}C age calibration program, *Radicarbon,* **35,** 215–230.

Tushingham, A.M. & Peltier, W.R., 1991. Ice-3G: a new approach of the late Pleistocene deglaciation based upon geophysical predictions of post-glacial relative sea level change, *J. geophys. Res.,* **96,** 4497–4523.

Wieczerkowski, K., 1999. *Gravito-Viskoelastodynamik für verallgemeinerte Rheologien mit Anwendung auf den Jupitermond Io und die Erde*, Series C, No. 515, Verlag der Bayerischen Akademie der Wissenschaften, München.

Wieczerkowski, K., Mitrovica, J.X. & Wolf, D., 1999. A revised relaxation-time spectrum for Fennoscandia, *Geophys. J. Int.,* **139,** 69–86.

Wolf, D., 1996. Note on estimates of the glacial-isostatic decay spectrum for Fennoscandia, *Geophys. J. Int.,* **127,** 801–805.

Wolf, D., Hagedoorn, J. & Martinec, Z., 2002. A new time-domain method of implementing the sea-level equation in glacial-isostatic adjustment, *EOS, Trans. Am. geophys. Un.,* **83,** Fall Meet. Suppl., G12A–1059.